# Analysis of a micropolarizer array-based simultaneous phase-shifting interferometer

Matt Novak, James Millerd, Neal Brock, Michael North-Morris, John Hayes, and James Wyant

Recent technological innovations have enabled the development of a new class of dynamic (vibration-insensitive) interferometer based on a CCD pixel-level phase-shifting approach. We present theoretical and experimental results for an interferometer based on this pixelated phase-shifting technique. Analyses of component errors and instrument functionality are presented. We show that the majority of error sources cause relatively small magnitude peak-to-valley errors in measurement of the order of 0.002–0.005λ. These errors are largely mitigated by high-rate data acquisition and consequent data averaging. © 2005 Optical Society of America

*OCIS codes:* 120.3180, 120.5050.

## 1. Introduction

Phase-shifting interferometry has become ubiquitous for the measurement and characterization of many types of surfaces including lenses, mirrors, and aspheres, with various techniques available for analysis of interference data.[1–4] The inherent limitations imposed by vibration in traditional temporal phase-shifting interferometers have been under investigation for some time.[5,6] In response to these imposed limitations, there has been a great deal of work done in the areas of vibration sensitivity suppression as well as exploring vibration-insensitive instantaneous phase-shifting interferometry.[7–16] Recent advances in computing and electronic circuit capability as well as technological advances in microfabrication techniques have facilitated the development of new technology for the implementation of a new type of instantaneous phase measurement system. Systems based on the technology presented provide a means to make instantaneous phase measurements in broad spectrum applications, which may enable short coherence sources to be used and scanning and profiling-type systems with broadband or white-light sources to be created. Also, the technology can be used as a facilitator for dynamic interferometry in vibration-rich environments such as machining and manufacturing areas, optical shops, or in environments with large airflow or other vibration constraints. This system, based on a micropolarizer array phase-shifting approach, enables simultaneous acquisition of the phase-shifted frames using a spatially applied carrier phase shift at the CCD pixel level. Because the data for phase calculations are collected during a time scale much smaller than the vast majority of laboratory and production environment vibrations, the effects of the vibration on the phase measurement are essentially frozen in time. This fact makes this system largely insensitive to the effects of vibration. To explore the performance capabilities and limitations of the phase sensor, both Twyman–Green and Fizeau-type interferometers were constructed to enable laboratory experimentation with this phase-shifting method. Also, theoretical analyses relating to this pixelated phase mask method were made. In this work, some theoretical analyses are presented, followed by experimental data showing various system performance metrics such as a phase-step response for the system and the mitigating effects of the averaging of the measurements. From the experimentation and modeling work, some conclusions are drawn regarding the limiting factors involved in phase measurements made with this technique.

M. Novak (mnovak@optics.arizona.edu) and J. Wyant are with the Optical Sciences Center, University of Arizona, Tucson, Arizona 85721. J. Millerd, N. Brock, M. North-Morris, and J. Hayes are with 4D Technology Corporation, 3280 East Hemisphere Loop, Suite 146, Tucson, Arizona 85706.

Received 12 January 2005; revised manuscript received 18 May 2005; accepted 27 June 2005.

0003-6935/05/326861-08$15.00/0

## 2. Experimental Setup

The fundamental setup for experimentation is a polarization-based Twyman–Green interferometer with a helium–neon laser source (632.8 nm). A diagram of this type of interferometer is shown in Fig. 1.

The interferometer was constructed under a positive-flow clean hood to mitigate the effects of dust and contaminants on the optical setup. The coherent noise brought about by scattering in the instrument was thus minimized. The He–Ne laser source is spatially filtered and collimated and then passed through a half-wave retarder used to balance the irradiance in each beam of the interferometer. Depending on the reflectivity of the test sample, the half-wave retarder is rotated to achieve an equal irradiance in the two interfering beams. A polarizing beam-splitter (PBS) cube then reflects a portion of the incident field and transmits the remaining portion of the beam. Quarter-wave-plate (QWP) linear retarders with their fast axes oriented at 45° then transform the linear polarized light into right- and left-hand circular polarized light in the two interferometer arms. These circular polarized reference and test beams are then reflected from flat mirrors and passed again through the QWPs, transforming each into the corresponding orthogonal linear component. In this way, the light that was originally transmitted by the PBS is now reflected, and the reflected light is now transmitted. The beams, recombined, then pass on to the phase-sensor portion of the setup. Here, another QWP is used to transform the linear light into orthogonal circular components, which are then phase shifted via the polarizing wire grids in the pixelated mask.

## 3. Dynamic Interferometer Phase-Sensor Basics

First we provide a basic description of the dynamic phase sensor specific to our chosen implementation for the work presented here. The fundamental idea is to introduce at each pixel a spatially varying known phase shift to the two beams incident on the phase sensor. At the pixel level, the beams will undergo known phase shifts relative to one another depending on the arrangement of the shift for each of the pixels at the corresponding camera location. After the orthogonally polarized reference and test beams have been recombined and sent to the phase measurement portion of the interferometer as described in Section 1, the phase-shift portion of the measurement sequence takes place. Background on the principle of the phase shift will be provided next.

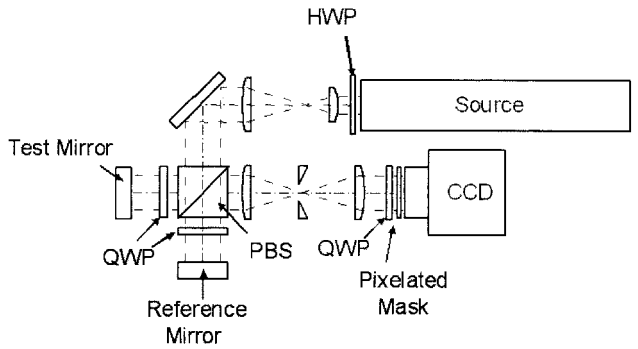


Fig. 1. Polarization-based Twyman–Green interferometer used for pixelated sensor experimentation. HWP, half-wave plate.

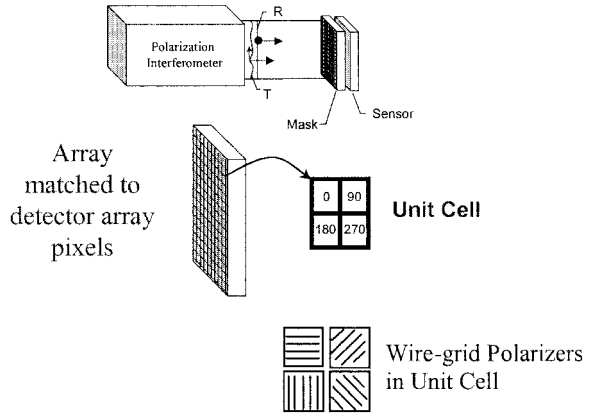


Fig. 2. Superpixel layout showing the phase-shift variation with pixel position.

It has been shown[17] that the irradiance following a linear polarizer for two incident orthogonal circular states is given by

$$I = \frac{1}{2}\left[I_r + I_l + 2\sqrt{I_r I_l}\cos(\Delta\phi + 2\theta)\right]. \quad (1)$$

Here $I$ is used to denote the total irradiance behind a linear polarizer oriented at angle $\theta$ for two incident circular polarized beams (denoted $r$ and $l$ for the right- and left-hand circular polarized electric fields of the reference and test beams in the interferometer from Fig. 1). The phase difference between the two beams originally input is $\Delta\phi$, which with a known reference corresponds directly with the phase of the test beam (the ultimate knowledge of which is the goal of the measurement). The phase shift introduced by the linear polarizer is proportional to the orientation of the polarizer angle $\theta$ and is given by $2\theta$. This proves to be a powerful means with which to manipulate the phase of the beams in an interferometer on a pixel-by-pixel basis and serves as the foundation for the pixelated phase mask sensor.

Using this fact, a mask has been fabricated such that the irradiance is manipulated at each pixel using a known polarizer angle to produce the desired phase shifts. These linear polarizers are wire grids with an approximate 150 nm period, with the wires set at angles of 0°, 45°, 90°, and 135° for the four desired phase-shift values. The phase shifts introduced then correspond to a 0°, 90°, 180°, and 270° relative phase between the test and the reference beams. Once this phase-shifting scheme is implemented, conventional four-bucket phase calculation algorithms can be used to determine the wavefront phase at a particular point on the wavefront, provided that the local slopes are not too great. Figure 2 shows the basic sensor principal.

Using this type of phase sensor, the test wavefront

phase at points across the CCD may then be calculated. One basic calculation equation is shown as Eq. (2), where irradiance values at each given pixel are used to calculate the tangent of the test beam phase to within a $2\pi$ ambiguity:

$$\tan(\phi) = \frac{I_{0^\circ} - I_{180^\circ}}{I_{90^\circ} - I_{270^\circ}}. \quad (2)$$

#### 4. Phase Calculations and Error Analyses

Next some error analyses that are specific to this particular method of dynamic interferometry are presented. Some similar work has been presented elsewhere; we show these calculations for completeness. The phase calculation made with this methodology is inherently subject to errors associated with the assumption that the phase is constant over a finite region where in fact this may not be (generally is not) the case. For example, if we calculate the phase using a $2 \times 2$ grid of pixels such as that shown in Fig. 2, then it is assumed that the phase of the test wavefront is constant over this area to make the calculation. This is not necessarily true and results in errors in the calculated phase value. When the phase is calculated with a four-bucket approach or a weighted average approach, the errors can be plotted as a function of input phase to study the effects.

Two models were created to study these effects. This was accomplished by modeling a tilted wavefront across an array of four or nine pixels associated with superpixels composed of $2 \times 2$ or $3 \times 3$ grids. The associated phase calculation was then made for varying degrees of tilt. For the $2 \times 2$ calculation, Eq. (2) is sufficient. The $3 \times 3$ calculation is only slightly more complex. Each of the components of the phase is determined by a weighted average that is calculated as the $3 \times 3$ pixel grid is examined across the entire data array. The $3 \times 3$ grid looks like a repetition of the several various phase shifts with either one, two, or four components added and averaged to give the true value at the center of the $3 \times 3$ grid. One form of this grid (there is a different permutation of the grid depending on the grid center pixel) is shown in Fig. 3.

This phase grid is repeated over the extent of the CCD array used to do the imaging and measurement in the interferometer. As can be seen from Fig. 3, there are four common sine terms, two similar cosine and sine terms, and also one cosine term that stands alone with the highest weight for this particular grid (the center point in the grid has a weight of 1.0 for the calculation). Equation (3) shows the calculation for this $3 \times 3$ pixel arrangement:

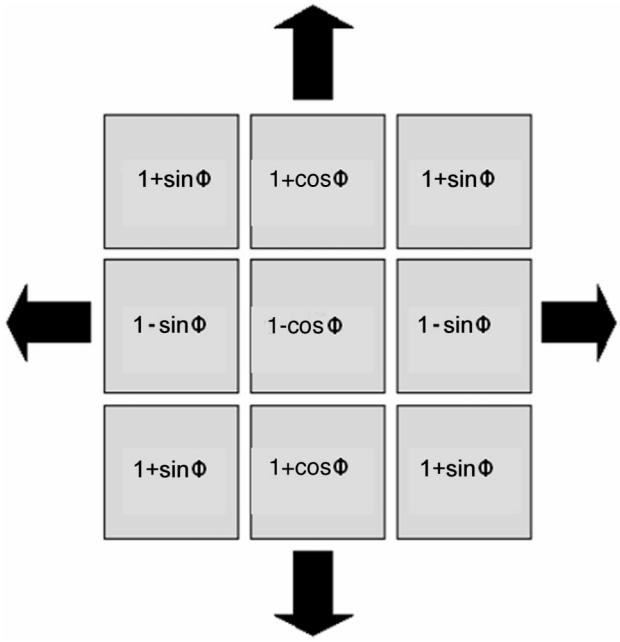


Fig. 3. Phase grid for $3 \times 3$ weighted average phase calculation.

Here the indices refer to the row and column number of the pixel in the $3 \times 3$ grid, respectively. The 2,2 pixel containing the cosine term is shown in the denominator with the weight of 1.0; the other weights are distributed according to the average for each case determined by the number of similar pixels in the grid. We present the phase calculation errors for two different organizations of this grid, namely, a stacked orientation where 180° out-of-phase terms are vertically spaced and a circular orientation where the 180° out-of-phase terms are located diagonally across and displaced by one row in the matrix. Similar errors due to tilt and consequent methods of compensation have been explored for conventional phase-shifting interferometry. Here we show the analogous effect for the pixelated phase-shift approach. The calculations shown are representative of the errors seen for the case of a tilted wavefront across the aperture of the instrument. The magnitude of tilt per pixel affects the magnitude of the error in the phase measurement. From Figs. 4(a) and 4(b) we see that the phase-dependent error is approximately an order of magnitude larger for the stacked algorithm calculation than for the circular algorithm calculation.

There are other sources of error associated with the instrument under study. Some of the interesting sources of error include polarizer angle and extinc-

$$\tan(\phi) = \frac{1/4\,(4 + \sin[\phi_{1,1}] + \sin[\phi_{1,3}] + \sin[\phi_{3,1}] + \sin[\phi_{3,3}]) - 1/2\,(2 - \sin[\phi_{2,1}] - \sin[\phi_{2,3}])}{1/2\,(2 + \cos[\phi_{1,2}] + \cos[\phi_{3,2}]) - (1 - \cos[\phi_{2,2}])}. \quad (3)$$

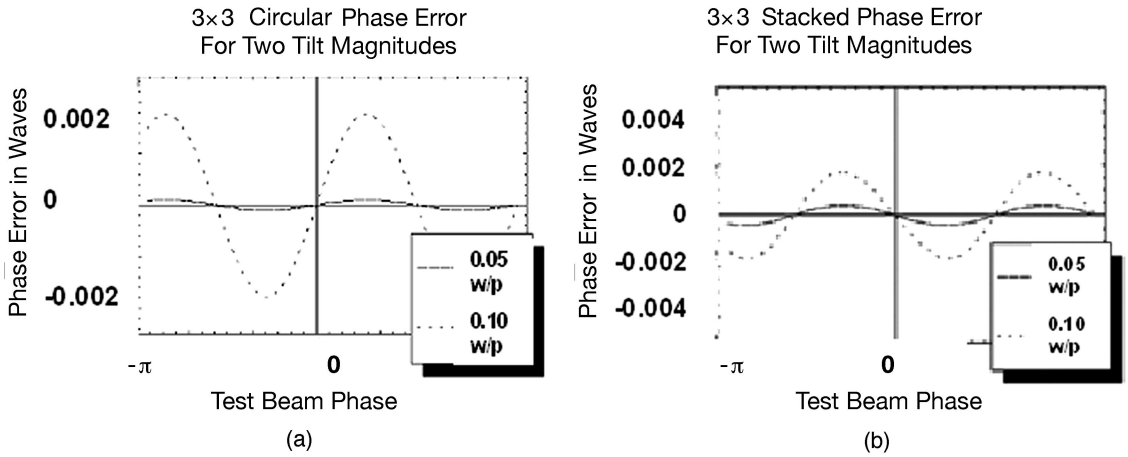


Fig. 4. (a) $3 \times 3$ circular pixel grid algorithm showing the corresponding expected error. (b) $3 \times 3$ stacked pixel grid algorithm showing the corresponding expected error. w/p, waves per pixel.

tion errors, errors in retardance for the wave plates used to create the orthogonally polarized reference and test states, and instrument retrace error. Next we present analyses related to each of these effects.

### A. Quarter-Wave-Plate Retardance Errors

We examine next the effects of imperfect retarders in the formation of the circularly polarized orthogonal reference and test beams. It is often the case that the retardance for such elements is out of specification by a few percent, up to as much as 15%–20% for poorly fabricated parts. In this subsection we look at the effects of such errors on the phase calculation.

To make the calculation analyses necessary to determine the effects of QWP errors, a closed-form expression for the matrix form of a rotated linear retarder was sought, including errors in axis orientation for the wave plates, and as well errors in the retardance values of the wave plates. This matrix is shown in Eq. (4):

$$M = \begin{bmatrix} \exp[1/2\, i\, (\delta+\phi)]\left\{\cos^2\left[\frac{\pi\varepsilon}{180}+\theta\right] + \exp[1/2\, i\, (\delta+\phi)]\sin^2\left[\frac{\pi\varepsilon}{180}+\theta\right]\right\} & \\ \quad - i \sin\left[\frac{\pi\varepsilon}{90}+2\theta\right]\sin\left[\frac{\delta+\phi}{2}\right] & - i \sin\left[\frac{\pi\varepsilon}{90}+2\theta\right]\sin\left[\frac{\delta+\phi}{2}\right] \\ \exp[-1/2\, i\, (\delta+\phi)]\left\{\exp[i\, (\delta+\phi)]\cos^2\left[\frac{\pi\varepsilon}{180}+\theta\right] + \sin^2\left[\frac{\pi\varepsilon}{180}+\theta\right]\right\} & \end{bmatrix}. \quad (4)$$

In this matrix the retardance of the wave plate is represented as $\phi$. The error in the retardance is $\delta$. The symbol $\theta$ is used to denote the orientation of the fast axis of the retarder, and $\varepsilon$ is the error in this orientation. Using this form of the rotated retarder, the amplitudes of the electric field for each pixel in a pixelated mask-based interferometer were then calculated in the presence of various errors. For the case of axis alignment, the results were not critically affected. For the case of retardance variation, we see results that may prove significant for even small values of retardation error. The key then is to understand the possible magnitude of the effect and also the mitigating factors and averaging capability of the interferometer. To illustrate the effects, the error in calculated phase is plotted against $\phi_t$ (the unknown test phase) for two values of retardance error. The plots are shown in Fig. 5.

As can be seen from Fig. 5, an error of $\lambda/20$ in retardance produces approximately $0.007\lambda$ peak-to-valley error in the calculated phase. The magnitude of these errors is consistent with functional instrument performance, and the effect it has on phase measurement can be mitigated to a large extent by averaging. This key benefit of a high data-acquisition rate may be utilized to reduce the error associated with phase-dependent errors of many types, independent of error cause. This is due to the fact that, as vibration tends to move the starting phase (via piston) for the test wavefront, several mea-

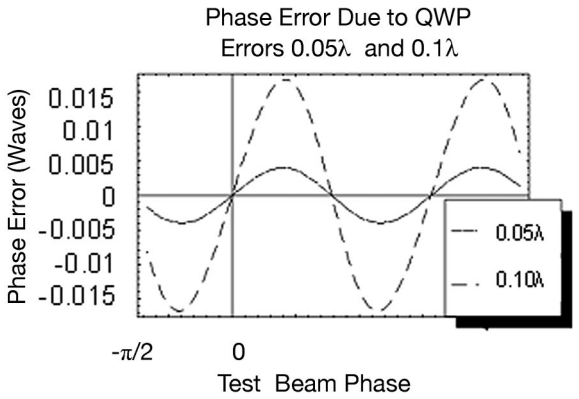


Fig. 5. Error in calculated phase for QWP retardance errors of 0.05λ and 0.1λ.

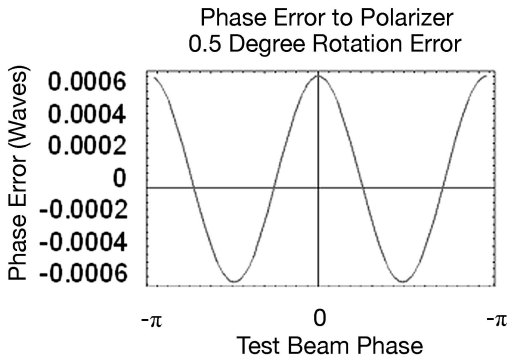


Fig. 6. Phase error due to 45° polarizer misalignment.

surements may be made and averaged to null out the effects of these types of phase-dependent error.

### B. Polarizer-Related Errors

Next we examine the effects of variations in the polarizing elements used in the interferometer. Since the phase shift produced for each pixel is dependent on the linear polarizer orientation and also the irradiance at the pixel, it is useful to understand how variation in the polarizers affects the phase measurement capability of the interferometer.

#### *1. Polarizer Alignment Errors*

The alignment of the polarizers in the mask with respect to the local Cartesian coordinate system determines the phase shift imparted to the light incident on the polarizer. This was shown in Eq. (1). If one or more of the polarizers is oriented at an angle other than optimum for the phase shift desired, there will be an error in the phase shift produced by the mask at that point. In Fig. 6 we present one such phase-dependent error, in this case for misalignment of the 45° polarizing wire grid. This error would arise in the instrument if the wire-grid polarizer oriented at a 45° nominal axis angle was misaligned during the fabrication of the mask.

The magnitude of the error associated with a 0.5° polarizer misalignment suggests that this will not be a significant contribution to overall instrument error. This is due to the fact that the error is approximately 1 order of magnitude smaller than the errors associated with QWP axis misalignment and would likely be masked by the larger errors associated with other system components. It is also likely that a 0.5° alignment error would not be overlooked during the polarizer fabrication process, implying that the actual errors to be expected due to polarizer alignment may be smaller still. These errors would then likewise be mitigated to a large extent by averaging during measurement.

#### *2. Polarizer Extinction Ratio Errors*

Next we examine more closely the effects of imperfect diattenuation for the wire-grid polarizers used in the instrument. This imperfection manifests itself mainly in the failure to completely extinguish light that should be blocked by the polarizer due to its $E$ field orientation. As stated previously, this leads to stray amplitude and phase light entering into pixels and contributing to an irradiance error at that pixel. In this subsection we examine the effects of these imperfections on measurement capability.

A perfect linear polarizer will exhibit a diattenuation of 1.0, where the polarizer passes with 100% efficiency radiation aligned with its preferred direction and blocks 100% of the radiation polarized in the orthogonal sense. We examine two cases, first the case of equal, nonideal diattenuation for the polarizers. Second, we examine the effects for uniform polarizers in three of the four pixels making up a 2 × 2 superpixel. In the first case, we see only a modulation effect; in the second, we see a nonlinear error in the phase calculation.

To examine these effects, a matrix form for the general linear polarizer with diattenuation coefficient $\alpha$ and orientation angle $\theta$ was derived. This matrix form is shown in Eq. (5):

$$D = \begin{bmatrix} (1-\alpha)\cos^2[\theta] + \alpha \sin^2[\theta] & (1-\alpha)\cos[\theta]\sin[\theta] - \alpha \sin[\theta]\cos[\theta] \\ (1-\alpha)\cos[\theta]\sin[\theta] - \alpha \sin[\theta]\cos[\theta] & \alpha \cos^2[\theta] + (1-\alpha)\sin^2[\theta] \end{bmatrix}. \quad (5)$$

In the matrix $D$, $\theta$ represents the angle of the polarizer axis from horizontal and $\alpha$ represents the diattenuation factor difference from 1.0. A 90% diattenuator would then have a value of 0.1 for $\alpha$.

To examine the situation, the effect of a 90% diattenuator in the place of perfect polarizers for each subpixel in a superpixel was examined. Using the

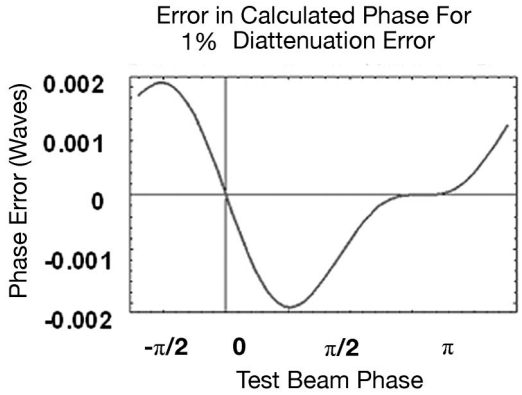


Fig. 7. Phase-dependent error plot for $\alpha = 0.01$ linear diattenuator.

appropriate values for $\theta$ as described previously, appropriate phase shifts are introduced at each of the pixels making up a superpixel. Equations (6) show the four irradiance values calculated theoretically in this case for a general test wavefront phase $\phi_t$ for a diattenuation coefficient $\alpha = 0.1$, given the four different polarizer angles for a $2 \times 2$ superpixel:

$$\begin{aligned} I_1 &= 0.82 + 0.8 \sin[\phi_t], \\ I_2 &= 0.82 + 0.8 \cos[\phi_t], \\ I_3 &= 0.82 - 0.8 \sin[\phi_t], \\ I_4 &= 0.82 - 0.8 \cos[\phi_t]. \end{aligned} \tag{6}$$

As can be seen from these functional forms of the irradiance, the net effect is a decrease in the fringe contrast (noted by the less than unity coefficients for the sinusoidal terms). However, if one uses standard four-bucket techniques to calculate the phase of the test beam from these irradiance values [see Eq. (2)], one obtains directly $\tan[\phi_t]$. The effect is therefore one of reduced fringe contrast. For this relatively high value of $\alpha$ (0.1 in this case), the modulation is reduced by 20% from the ideal situation.

The error in calculation becomes more pronounced when there are different diattenuation factors associated with the polarizers for each pixel in the group. To examine this case, we present the effect of one of the superpixel quadrants exhibiting a high level of diattenuation imperfection while the other quadrants are treated as perfect linear polarizers. This would be analogous to an error in the processing of one of the polarizer pixel elements during the mask fabrication process. Since each of the pixel orientations is fabricated all at once and independently from the other pixel types in the mask, it is possible to have a defect inherent to one of the process steps that would lead to this type of effect. The result is that the process error affects only one of the polarizer types in the pixelated mask, and there is a resulting phase-dependent error. This phase-dependent error is plotted in Fig. 7.

In this plot the phase is plotted over a span of $2\pi$ rad, and the error is seen to peak at approximately $0.002\lambda$ for diattenuation $\alpha = 0.1$. The form of the error exhibits some characteristics similar to nonlinear detector errors. The magnitude is such that it is realistic to expect this not to be a critical factor in instrument performance. Larger diattenuation imperfections could become detrimental to measurement accuracy and should therefore be avoided by ensuring the accuracy of the polarizer fabrication process.

## 5. Experimentation

Next we discuss the irradiance step response and present experimental results related to the phase-step response and reduction of error components through averaging. These metrics are good indicators of interferometer performance.

### A. Irradiance Step Response

The irradiance step response can be thought of as the effect of the edge of the test part on the measurement. For a $2 \times 2$ pixel grid calculation, the edge pixel must be removed from the calculation (where there is no light from the test part reflected back into the interferometer). In the $3 \times 3$ case, this effect extends two pixels in from the edge. It is necessary to eliminate data from the edge so as to avoid ringing in the phase calculation at the edge of the optic under test, which would manifest as false surface error data.

### B. Phase-Step Response

One interesting instrument performance metric for an interferometer is the response to a phase step. The ideal response would occur over the span of one pixel, a simple binary transition from low to high phase. In practice, however, there are limitations due to the spatial nature of the phase calculation. In this subsection we present the calculation of phase for a perfectly input wavefront step subjected to the pixelated mask phase-shifting technique described, as well as actual experimental results for the response to a quarter-wave step.

The theoretical phase-step response was tested using a perfect quarter-wave step as the input to the phase calculation algorithm. Figure 8 shows a profile of the resulting phase-step output of the calculation algorithm. The slope of the calculated phase front shows this transition occurring over two pixels.

It is interesting to compare these theoretical calculations with experiment. A PhaseCam interferometer from 4D Technology was used to measure a quarter-wave step in the laboratory. To compare this result with the theoretical calculations, a cross section of the measurement shown was examined for the width of the transition of the phase step. The result is plotted in Fig. 9.

As can be seen, the experimental data agree well with the prediction of the two-pixel-wide phase-step response. This is inherent in the phase calculation mechanism due to the spatially separated nature of the phase-shift steps of the pixelated phase mask.

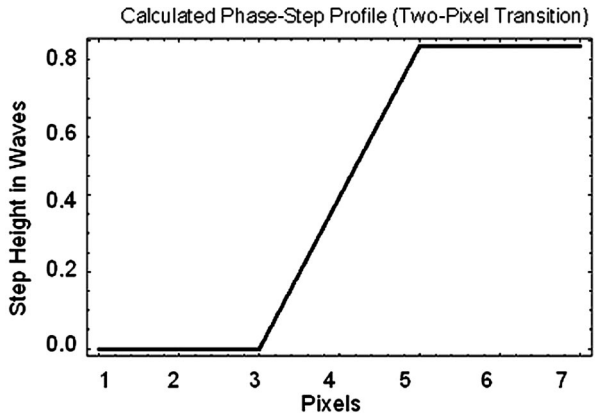


Fig. 8. Calculated phase-step transition showing a two-pixel transition.

### C. Mitigating Effects of Averaging

To show the effects of the error sources on real measurement data, a set of experiments were completed where a single measurement was compared with the averaged result of several measurements. To show that the phase-dependent errors can be nearly eliminated by averaging, we first made single measurements and then compared the results with an average of many consecutive (high-acquisition-rate) measurements. Through the piston of the starting phase inherent in the measurements due to vibration, the phase of the double-frequency error varies randomly; in the limit as we increase the number of measurements, the double-frequency fringes are reduced accordingly.

A flat mirror of good quality ($\lambda/20$ peak to valley) was measured for the following experiment. Figure 10 shows the straight tilt fringes obtained using a pixelated interferometer and this flat mirror in a standard Fizeau test configuration.

As can be seen from the fringes in Fig. 10, the mirror is relatively high quality and there is good fringe contrast. The measurements made here were performed under a positive pressure flow hood with some air turbulence and vibration inherent in the setup due to the airflow motor. A single measurement was taken and analyzed to show the effects of fringe print-through on the data. This result is shown in Fig. 11.

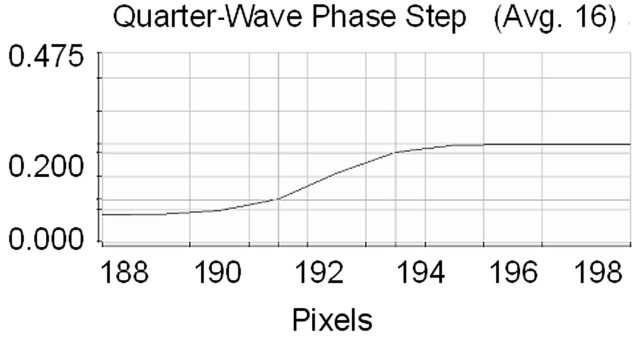


Fig. 9. Cross section of the phase-step measurement showing a two-pixel response as seen in the theoretical calculation.

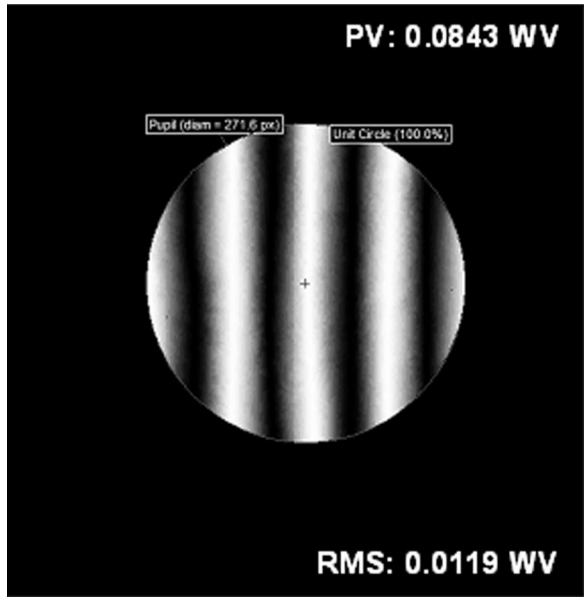


Fig. 10. Tilt fringes obtained from a flat mirror under test.

The double-frequency error is apparent here for the 3.5 fringes of tilt between the reference flat and the test mirror shown in Fig. 10. Here we see seven fringes of printthrough in this unaveraged single-measurement case. In theory, when several measurements are averaged one would expect to see a decreased sensitivity to this type of error. This is due to the change in the relative starting phase imparted by the vibration from the airflow hood or other environmental factors. This change in starting phase will

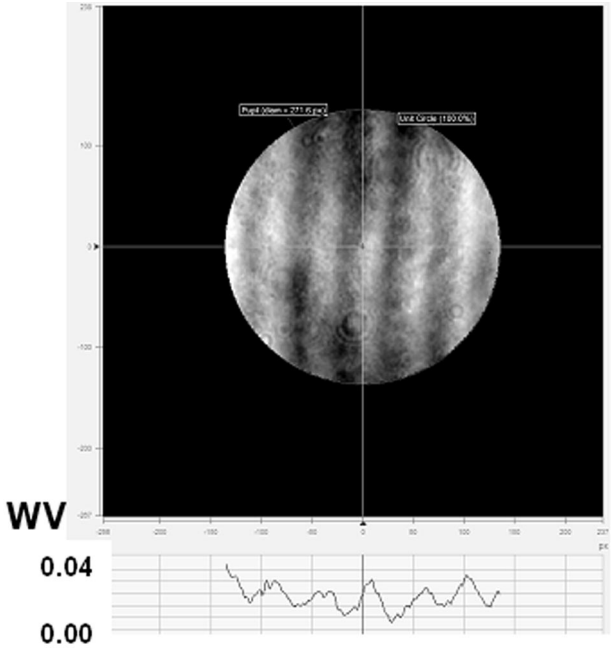


Fig. 11. Analysis of a single measurement of a flat mirror showing a double-frequency fringe print-through. WV, waves.

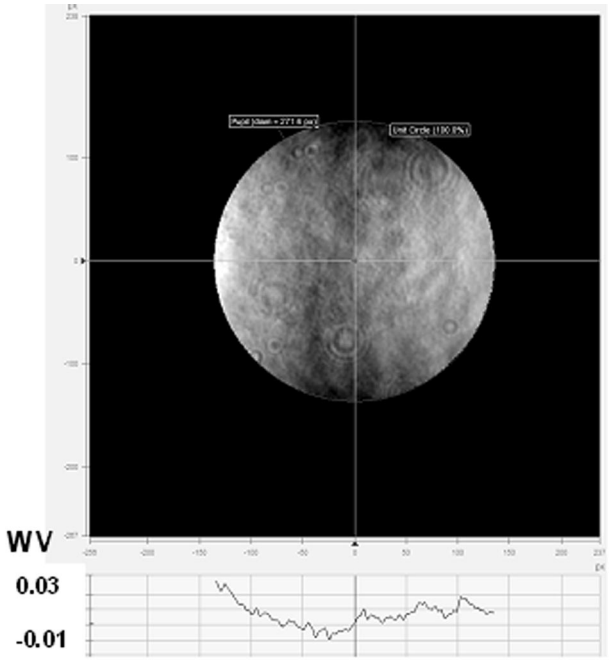


Fig. 12. Sixteen measurements of average data for a flat mirror. The double-frequency errors apparent in the unaveraged case have been greatly reduced.

in theory tend to cause an overall averaging to zero of the print-through. Figure 12 shows the resulting analysis data for an average of 16 measurements for the same optical surface under test.

As can be seen from Fig. 12, there is little if any remaining indication of double-frequency error in the data. The overall shape of the surface remains the same with a peak-to-valley error of the order of $\lambda/20$. However, the sinusoidal shape of the print-through has been averaged out from the resulting data.

## 6. Conclusions

We have shown both theoretical and experimental performance for a micropolarizer array-based simultaneous phase-shifting interferometer. We have demonstrated a theoretical phase-step response and experimental agreement with the theoretical value of the response. Calculation-based and also component-based limitations to the values of the measured wavefront phase have been shown, and we demonstrated that component errors introduce errors comparable in magnitude to phase calculation errors. We then showed that to a great extent the effects of the component errors may be mitigated by the averaging of several measurements, enabled by the high rate of data acquisition of the vibration-insensitive system. This suggests that an overall performance limitation may be found in the stray radiation due to diffraction or other stray-light sources in the system.

We extend our gratitude to 4D Technology, Inc., for support of this work.

## References

1. K. Creath, "Phase measurement interferometry techniques," Prog. Opt. **26,** 349–393 (1988).
2. K. Creath and J. C. Wyant, "Direct phase measurement of aspheric surface contours," in Proc. SPIE **645,** 101–106 (1986).
3. D. Malacara, M. Servin, and Z. Malacara, *Interferogram Analysis for Optical Testing* (Marcel Dekker, 1998).
4. J. E. Greivenkamp and J. H. Bruning, "Phase-shifting interferometry," in *Optical Shop Testing,* D. Malacara, ed. (Wiley, 1992), pp. 501–598.
5. J. Schwider, "Phase shifting interferometry: reference phase error reduction," Appl. Opt. **28,** 3889–3892 (1989).
6. J. Schwider, T. Dresel, and B. Manzke, "Some considerations of reduction of reference phase error in phase-stepping interferometry," Appl. Opt. **38,** 655–659 (1999).
7. R. Smythe and R. Moore, "Instantaneous phase measuring interferometry," Opt. Eng. **23,** 361–364 (1984).
8. P. J. De-Groot and L. L. Deck, "Numerical simulations of vibration in phase-shifting interferometry," Appl. Opt. **35,** 2172–2178 (1996).
9. O. Kwon, "Multichannel phase-shifted interferometer," Opt. Lett. **9,** 59–61 (1984).
10. L. P. M. Melozzi and A. Mazzoni, "Vibration-insensitive interferometer for on-line measurements," Appl. Opt. **34,** 5595–5601 (1995).
11. J. McLaughlin and B. Horwitz, "Real-time snapshot interferometer," in Proc. SPIE **680,** 35–43 (1986).
12. M. Kuechel, "The new Zeiss interferometer," in Proc. SPIE **1332,** 655–663 (1990).
13. C. Koliopoulis, "Simultaneous phase-shift interferometer," in Proc. SPIE **1531,** 119–127 (1992).
14. B. K. A. Ngoi, K. Venkatakrishnan, N. R. Sivakumar, and T. Bo, "Instantaneous phase shifting arrangement for microsurface profiling of flat surfaces," Opt. Commun. **190,** 109–116 (2001).
15. B. K. A. Ngoi, K. Venkatakrishnan, and N. R. Sivakumar, "Phase-shifting interferometry immune to vibration," Appl. Opt. **40,** 3211–3214 (2001).
16. J. Millerd, N. Brock, J. Hayes, M. North-Morris, M. Novak, and J. C. Wyant, "Pixelated phase-mask dynamic interferometer," in Proc. SPIE **5531,** 304–314 (2004).
17. M. P. Kothiyal and R. Delisle, "Shearing interferometer for phase shifting interferometry with polarization phase shifter," Appl. Opt. **24,** 4439–4442 (1985).